A Comprehensive Characterization of Empirical Parameterizations for OH Exposure in the Aerodyne Potential Aerosol Mass Oxidation Flow Reactor (PAM-OFR)

Qianying Liu[1,2], Dan Dan Huang[2,*], Andrew T. Lambe[3], Shengrong Lou[2], Lulu Zeng[1], Yuhang Wu[2], Congyan Huang[2], Shikang Tao[2], Xi Cheng[4], Qi Chen[5], Ka In Hoi[1], Hongli Wang[2], Kai Meng Mok[1], Cheng Huang[2,6], Yong Jie Li[1,*]

[1]Department of Civil and Environmental Engineering, Department of Ocean Science and Technology, and Centre for Regional Oceans, Faculty of Science and Technology, University of Macau, Taipa, Macau SAR, 999078, China
[2]State Environmental Protection Key Laboratory of Formation and Prevention of Urban Air Pollution Complex, Shanghai Academy of Environmental Sciences, Shanghai, 200233, China
[3]Aerodyne Research Inc., Billerica, Massachusetts, 01821, United States
[4]School of Chemical and Environmental Engineering, China University of Mining and Technology (Beijing), Beijing 100083, China
[5]State Key Joint Laboratory of Environmental Simulation and Pollution Control, BIC-ESAT and IJRC, College of Environmental Sciences and Engineering, Peking University, Beijing, China
[6]State Ecology and Environment Scientific Observation and Research Station for the Yangtze River Delta at Dianshan Lake，Shanghai Environmental Monitoring Center, Shanghai, 200030, China

Correspondence to: Dan Dan Huang (huangdd@saes.sh.cn), Yong Jie Li (yongjieli@um.edu.mo)

Abstract. The oxidation flow reactor (OFR) has been widely used to simulate secondary organic aerosol (SOA) formation in laboratory and field studies. OH exposure (OH_{exp}), representing the extent of hydroxyl radical (OH) oxidation and normally expressed as the product of OH concentration and residence time in the OFR, is important in assessing the oxidation chemistry in SOA formation. Several models have been developed to quantify the OH_{exp} in OFRs, and empirical equations have been proposed to parameterize OH_{exp}. Practically, the empirical equations and the associated parameters are derived under atmospheric relevant conditions (i.e., external OH reactivity) with limited variations of calibration conditions, such as residence time, water vapor mixing ratio, O_3 concentration, etc. Whether the equations or parameters derived under limited sets of calibration conditions can accurately predict the OH_{exp} under dynamically changing experimental conditions with large variations (i.e., extremely high external OH reactivity) in real applications remains uncertain. In this study, we conducted 62 sets of experiments (416 data points) under a wide range of experimental conditions to evaluate the scope of the application of the empirical equations to estimate OH_{exp}. Sensitivity tests were also conducted to obtain a minimum number of data points that is necessary for generating the fitting parameters. We showed that, for the OFR185 mode (185-nm lamps with internal O_3 generation), except for external OH reactivity, the parameters obtained within a narrow range of calibration conditions can be extended to estimate the OH_{exp} when the experiments are in wider ranges of conditions. For example, parameters derived within a narrow water vapor mixing ratio range (0.49–0.99 %, corresponding to 15.1–30.8 % of relative humidity at 101.325 kPa and 298 K) can be extended to estimate the OH_{exp} under the entire range of water vapor mixing ratios (0.49–2.76 %,

equivalent to 15.1–85.7 % of relative humidity under identical conditions). However, the parameters obtained when the external OH reactivity is below 23 s^{-1} could not be used to reproduce the OH_{exp} under the entire range of external OH reactivity (4–204 s^{-1}). For the OFR254 mode (254-nm lamps with external O_3 generation), all parameters obtained within a narrow range of conditions can be used to estimate OH_{exp} accurately when experimental conditions are extended. Additionally, when using the OFR254 mode, too-low lamp voltages should be avoided, as they will generally result in large deviations in the estimations of OH_{exp} from empirical equations. Regardless of OFR185 or OFR254 mode, at least 20–30 data points from sulfur dioxide (SO_2) or (carbon monoxide) CO decay with varying conditions are required to fit a set of empirical parameters that can accurately estimate OH_{exp}. Caution should be exercised to use fitted parameters from low external OH reactivity to high ones, for instance, those from direct emissions such as vehicular exhaust and biomass burning.

1 Introduction

As the most important oxidant in tropospheric chemistry (Ehhalt, 1999), hydroxyl (OH) radical is vital in oxidizing primary pollutants such as volatile organic compounds (VOCs) and contributes to secondary organic aerosol (SOA) and tropospheric ozone (O_3) formation. The OH radical has daytime concentrations of 10^5 to 10^7 molecules cm^{-3}, exhibiting daily (Cao et al., 2020; Tan et al., 2017), seasonal (Friedman and Farmer, 2018), as well as spatial (Cao et al., 2020; Stone et al., 2012) variations. An average daily OH radical concentration of 1.5×10^6 molecules cm^{-3} is widely used to estimate the photochemical age of an air mass (Mao et al., 2009). Typical VOCs have second-order rate constants of 10^{-15} to 10^{-10} cm^3 $molecule^{-1}$ s^{-1} with OH radicals (Atkinson and Arey, 2003; Atkinson et al., 2006), which can be translated to atmospheric lifetimes of hours to approximately a year (Seinfeld and Pandis, 2016). This situation poses challenges in laboratory experiments to directly simulate the OH oxidation of VOCs, which is one of the most important chemical processes in the Earth's atmosphere.

Smog chambers (Cocker et al., 2001; Hildebrandt et al., 2009; Wang et al., 2014) and oxidation flow reactors (OFRs) (George et al., 2007; Kang et al., 2007; Lambe et al., 2011) have been widely employed to simulate oxidation of VOCs and subsequent SOA formation. For example, the Caltech Chamber provides oxidation conditions close to the real atmosphere, making it suitable for the study of complex multi-step reactions and low-volatility products. However, each experiment takes several hours to days and long-duration experiments are prone to background interference. The Toronto Photo-Oxidation Tube (TPOT) focuses on the study of heterogeneous oxidation reactions of aerosols. Its 0.8 L volume makes it portable, but it is prone to uneven residence time distribution (RTD) and significant wall effects. The Potential Aerosol Mass Oxidation Flow Reactor (PAM-OFR) and the Gothenburg Potential Aerosol Mass Oxidation Flow Reactor (Go: PAM-OFR) are often used to study the transformation of gaseous precursors into particles (such as the formation of SOA). The Go: PAM-OFR has a volume of 7.2 L, which is only half that of the PAM-OFR, making it suitable for experiments on mobile platforms. However, its small volume gives it the same disadvantages as the TPOT, and it is equipped with only a single UV lamp, which does not allow for as wide a range of controllable oxidation levels as the PAM-OFR. The PAM's moderate volume and central flow sampling can reduce wall effects.

These OFRs of reactors normally operate with high concentrations of oxidants (e.g., OH radicals), which lead to a significant acceleration of oxidation reactions, often by orders of magnitude. To reconcile the differences in OH concentration and exposure time between ambient and laboratory settings, the oxidation extent, i.e., OH exposure (OH_{exp}, molecules cm^{-3} s) is normally used to extrapolate laboratory findings to ambient conditions. Despite drawbacks such as possible altered reaction mechanisms, this approach provides a quantitative assessment of the chemistry during OH oxidation in a reasonable time span and achievable detection capability. The OH_{exp} has a significant impact on the yield and product distribution during VOC oxidation (Cheng et al., 2021; Cheng et al., 2024). Accurate measurement or estimation of the OH_{exp} during laboratory experiments, therefore, is the key to understanding the oxidation chemistry that can represent the ambient conditions. In this study, we chose to further investigate the PAM-OFR to explore its OH_{exp}, as it offers moderate conditions in terms of experiment time, deployment complexity, range of oxidation levels, and wall effects.

The Aerodyne Potential Aerosol Mass OFR (PAM-OFR) is one of the most widely used OFRs for studying SOA formation and evolution (Zhang et al., 2024). It can achieve a wide range of atmospheric OH_{exp} conditions within short residence times on the order of minutes (Kang et al., 2007; Lambe et al., 2011). The PAM-OFR can be operated in a number of modes, depending on 1) the wavelength of the ultraviolet (UV) light source, 2) the concentration of the externally generated O_3 (if any), and 3) the injection of external precursor to generate NO_x (= NO + NO_2) or other oxidants (e.g., nitrate radical or halogen atoms) upon photolysis. The most widely used methods for OH generation include combined photolysis of O_2 and H_2O at λ = 185 nm plus photolysis of O_3 at λ = 254 nm (OFR185; R1–R6) or photolysis of externally added O_3 at λ = 254 nm (OFR254; R5–R6) (Rowe et al., 2020):

$$H_2O + h\nu_{185} \rightarrow H + OH \quad \text{(R1)}$$

$$H + O_2 \rightarrow HO_2 \quad \text{(R2)}$$

$$O_2 + h\nu_{185} \rightarrow 2O(^3P) \quad \text{(R3)}$$

$$O(^3P) + O_2 \rightarrow O_3 \quad \text{(R4)}$$

$$O_3 + h\nu_{254} \rightarrow O_2 + O(^1D) \quad \text{(R5)}$$

$$O(^1D) + H_2O \rightarrow 2OH \quad \text{(R6)}$$

To obtain the OH_{exp} under these two modes in the PAM-OFR, one can perform decay experiments on trace gases such as SO_2 and CO, and fit the OH_{exp} based on known second-order rate constants between OH radical and the trace gases, which is defined as $OH_{exp, dec}$. Based on the results of the decay experiments, Li et al. (2015) and Peng et al. (2015) developed estimation equations to parameterize OH_{exp} as a function of easily measurable quantities, which is denoted as $OH_{exp, est}$. A set of parameters (*a*–*f* and *x*–*z*, respectively) for the estimation equations of the OFR185 and OFR254 modes (see Sect. 2.3 for details) were obtained by fitting the estimation equations to $OH_{exp, dec}$ values obtained from decay experiments.

When using the PAM-OFR in field studies, it is necessary to obtain concurrent OH_{exp} that is representative of the ambient conditions. However, environmental conditions in field studies (e.g., humidity, temperature, etc.) are constantly changing, making it challenging to replicate these conditions for OH_{exp} estimation. In some field studies using PAM-OFR, concurrent OH_{exp} was estimated by measuring the relative decay of benzene and toluene (Liao et al., 2021; Liu et al., 2018). Additionally, some studies have mentioned that OH concentrations can be indirectly measured by detecting the decay of tracers such as 3-pentanol, 3-pentanone, pinonaldehyde, or butanol-d9 (Barmet et al., 2012). However, the measurement of all these organic tracers requires specific, sophisticated instruments such as proton-transfer-reaction time-of-flight mass spectrometers (PTR-MS). Additionally, switching the instrument back and forth between the front and end of the OFR during field measurements can result in some loss of real-time VOCs data before entering the OFR. To obtain accurate OH_{exp}, some studies explicitly modelled the radical chemistry in PAM-OFR (Li et al., 2015; Ono et al., 2014; Peng et al., 2015). The estimation equations developed by Li et al. (2015) and Peng et al. (2015), although empirical, reproduced the OH_{exp} from models within 10 %, making them a good choice because these equations only require the input of a few easily available parameters. Yet, it is unclear whether the fitted parameters obtained under certain conditions can still accurately estimate OH_{exp} when experimental conditions, such as UV light intensity, water vapor mixing ratio, residence time, and external OH reactivity (OHR_{ext}), undergo significant changes. Furthermore, there is currently no consensus on the minimum number of decay experiments required to obtain accurate parameterization for OH_{exp} estimation using these equations. This facet is important for field studies using PAM-OFR where only limited numbers of decay experiments can be done to obtain concurrent OH_{exp} estimation.

In this study, we conducted a series of experiments using the decay of SO_2 and CO to estimate the OH_{exp} in the PAM-OFR under OFR185 and OFR254 modes. The applicability of previously developed OH_{exp} estimation equations to obtain accurate OH_{exp} in the PAM-OFR has been evaluated by linear regression of $OH_{exp,\ est}$ against $OH_{exp,\ dec}$. We have also evaluated how well estimation equations perform when using limited ranges of experimental parameters (e.g., OHR_{ext}, residence time, water mixing ratio, etc.) or different trace gases (SO_2 and CO) and given recommendations. In addition, we have proposed the minimal number of trace-gas decay experiments required to obtain a set of usable parameters for the OH_{exp} estimation equations. Finally, we also compared the advantages and disadvantages of the OFR185 and the OFR254 modes from the perspective of the quantification of OH_{exp}. The methodology of this study can be applied to laboratory and field experiments for OH_{exp} estimation using PAM-OFR or other OFRs that follow a plug-flow assumption.

2 Methods

2.1 The PAM-OFR

Experiments were conducted using an Aerodyne PAM-OFR (Aerodyne Research Inc., Billerica, MA, US), which is a horizontal aluminium cylindrical chamber with an internal volume of 13.3 L. The PAM-OFR operates in a continuous flow mode. Four low-pressure Hg lamps are installed inside the reactor to produce UV light with characteristic spectral lines (e.g., 185 and 254 nm). The OH is generated via OFR185 using two ozone-producing Hg lamps (GPH436T5VH/4P, Light Sources,

Inc.) or via OFR254 using two ozone-free Hg lamps (GPH436T5L/4P, Light Sources, Inc.) to photolyze externally added ozone. A flow of nitrogen purge gas, ranging from 0.2 to 0.3 L min^{-1}, is introduced between the lamps and sleeves. This nitrogen gas flow serves to reduce the heat generated by the lamps and prevent the formation and accumulation of ozone between the lamps and the quartz tubes that isolate them from the sample flow in the OFR. A fluorescent dimming ballast is used to control the photon flux by regulating the voltage applied to the lamps, which allows us to generate different OH concentrations. In typical measurement sequences, nine lamp voltage settings (including lights off) were cycled through every 2–3 hours. The dimming voltage ranged from 0 to 10 V direct current (DC).

2.2 OH_{exp} estimation through decay of SO_2 and CO ($OH_{exp,\ dec}$)

OH_{exp} can be indirectly measured by detecting the decay of the tracers with known reaction rates. Inorganic trace gases SO_2 or CO react with OH radicals at slower rates compared to most VOCs. However, considering the complex oxidation chemistry of VOCs, SO_2 and CO can better capture the features of real OHR_{ext} decay and effective OHR_{ext} (Peng et al., 2015). We performed systematic decay experiments with SO_2 and CO in the PAM-OFR, with conditions tabulated in Tables S1 and S2. Figure S1 shows the schematics of the experimental setups in the OFR185 and OFR254 modes. In the OFR185 mode, the injected gas flow at the inlet of the PAM is made up of three sub-flows: (1) The trace-gas flow, i.e. SO_2 of 0.2–8.7 ppm or CO of 10.2–207.5 ppm supplied from gas cylinders (Purity: 99.9 % of SO_2, 99.95 % of CO; Shanghai Shenkai Gases Technology CO., LTD.); (2) dry clean air from a zero-air generator (ZAS-100/150, Convenient) with a non-methane hydrocarbon content of less than 1 ppb; (3) the humidified clean air passed through a Nafion humidifier (FC100-80-6MSS, Perma Pure). By adjusting the ratio of dry air to humidified air, the water vapor mixing ratio in the PAM-OFR can be controlled. Additionally, they also serve as makeup flows to maintain a constant flow rate. At the outlet of the reactor, the gas flow was sampled from an internal perforated Teflon ring. The gas-phase species (O_3, SO_2, and CO) were detected using an ultraviolet ozone analyser (UV-100, Eco Sensors), an SO_2 monitor (Model 43i, Thermo Scientific), and a CO monitor (G2401, Picarro), respectively. In the OFR254 mode, in addition to the previously mentioned setup, externally generated O_3 (through UV photolysis) with desired concentrations was injected at the inlet of the PAM-OFR.

Figures S2a and S2b depict examples of set and measured parameters during experiments conducted in the OFR185 and OFR254 modes, respectively. In the OFR185 mode, without radical generation to oxidize the tracer species, their concentration was allowed to stabilize under dark conditions. Once the concentration reached a steady state, the UV lamps were turned on. Different light intensities lead to varying levels of decay of SO_2 or CO after oxidation, reflecting different OH_{exp} within the PAM-OFR. In the OFR254 mode, it is necessary to obtain the initial concentration of O_3 injected into the PAM-OFR in the absence of OHR_{ext}. While waiting for the SO_2 or CO concentration to stabilize, the O_3 flow was temporarily blocked outside the PAM-OFR using a valve. Dry clean air was then introduced to compensate for this portion of the flow, ensuring a constant total flow throughout the entire process. Once the tracer species concentration had reached a steady state, the O_3 was then allowed to flow into the PAM-OFR. The total $OH_{exp,\ dec}$ in the reactor was varied over a wide range (approximately 10^9–10^{12} molecules cm^{-3} s) by changing the UV light intensity, water mixing ratio, and residence time. The mean residence time was

obtained from the ratio of the internal volume of and the total flow rate through the PAM-OFR. In the calculation of $OH_{exp,\ dec}$ (see the paragraph below), plug flow conditions were assumed, which has been shown to agree with the RTD approach for OH_{exp} when using species (such as SO_2 or CO) with low reaction rate constants with OH radicals ($k_{i,\ OH}$) by Li et al. (2015) and Peng et al. (2015).

$OH_{exp,\ dec}$ in the PAM-OFR was calculated from the pseudo-first-order reaction of OH with SO_2 or CO, whose $k_{i,\ OH}$ have been well characterized ($k_{SO2,\ OH}$ = 9.49 × 10^{-13} cm^3 $molecule^{-1}$ s^{-1} and $k_{CO,\ OH}$ = 2.4 × 10^{-13} cm^3 $molecule^{-1}$ s^{-1} at 1 atm and 298 K) (Burkholder et al., 2020; Cao et al., 2020). By measuring the decay of SO_2 or CO, the corresponding $OH_{exp,\ dec}$ is calculated as follows:

$$OH_{exp,\ dec} = \frac{-1}{k_{i,\ OH}} \times \ln\left(\frac{C_{i,\ out}}{C_{i,\ in}}\right) \quad (1)$$

where $c_{i,\ in}$ is the concentration of reactant *i* injected into the PAM-OFR (ppb), $c_{i,\ out}$ is reactant *i* concentration at the PAM-OFR outlet (ppb), and $k_{i,\ OH}$ is the second-order rate constant between the trace species (SO_2 or CO) and OH radicals.

Despite the use of nitrogen as a purge gas to reduce the heat generated by the lamp, temperature variations were still observed within the PAM-OFR. There was a maximum deviation of approximately 13 °C from 25 °C when using SO_2 as the OHR source. However, the $k_{SO2,\ OH}$ was 8.85 × 10^{-13} cm^3 $molecule^{-1}$ s^{-1} at 38 °C (Burkholder et al., 2020), which results in the calculated $OH_{exp,\ dec}$ being only approximately 7% higher than that derived from $k_{SO2,\ OH}$ at 25 °C. Pan et al. (2023) noted that temperature increases caused by lamp heating exerted minimal influence on gas-phase reaction rates, with SO_2 decay and OH exposure showing negligible variations. Therefore, the influence of temperature on reaction kinetics was not considered in this study.

2.3 OH_{exp} estimation from empirical equations ($OH_{exp,\ est}$)

Li et al. (2015) proposed an $OH_{exp,\ est}$ estimation equation (Eq. 2) for OFR185 based on easily measurable quantities:

$$OH_{exp,\ est} = 10^{\left[a+\left(b+c\times OHR_{ext}{}^{d}+e\times\log\left(O_{3,\ out}\times\frac{180}{t}\right)\times OHR_{ext}{}^{f}\right)\times\log\left(O_{3,\ out}\times\frac{180}{t}\right)+\log H_2O+\log\left(\frac{t}{180}\right)\right]} \quad (2)$$

where *a*–*f* are fitting parameters (values are reported in Table S5); $O_{3,\ out}$ is ozone concentration measured at the exit of the PAM-OFR (molecules cm^{-3}), which serves as a surrogate for UV flux; H_2O is water vapor mixing ratio in PAM-OFR (%), which is influenced by both temperature and relative humidity; t is mean residence time (s). The total external OH reactivity is represented by OHR_{ext} (s^{-1}) = $\sum_i k_i[C_i]$, where k_i and $[C_i]$ are the rate constants with OH and the concentration of the OH-consuming reactant *i* in the system (Wang et al., 2020).

Peng et al. (2015) proposed another equation (Eq. (3)) for $OH_{exp,\ est}$ in OFR254:

$$OH_{exp,\ est} = 10^{\left[x+\log(-\log r_{O_3})+y\times\left(\frac{OHR_{ext}}{O_{3,\ in}}\right)^{z}\right]} \quad (3)$$

where *x*–*z* are fitting parameters (values are reported in Table S6); log r_{O3} (log ($O_{3,\ out}/O_{3,\ in}$)) is the logarithm of the ratio between the output and input O_3 concentrations, which serves as a surrogate for UV flux and also captures the effect of H_2O; $O_{3,\ in}$ is the concentration of externally injected O_3 into the PAM-OFR (molecules cm^{-3}).

We have performed in total of 62 sets of trace-gas decay experiments with 416 data points for the $OH_{exp,\ dec}$, with 25 sets and 175 data points in the OFR185 mode and 37 sets and 241 data points in the OFR254 mode. In OFR185 mode, the 175 experiments cover an $OH_{exp,\ dec}$ range of 3.57×10^8–5.52×10^{12} molecules cm^{-3} s, with an equivalent photochemical age ranging from 4 minutes to 43 days. In OFR254 mode, the 241 experiments cover an $OH_{exp,\ dec}$ range of 1.01×10^9–2.18×10^{12} molecules cm^{-3} s, with an equivalent photochemical age ranging from 11 minutes to 17 days. The error in $OH_{exp,\ dec}$ is derived from the measurement error of the tracer gas, propagated through Eq. 1. When $OH_{exp,\ dec}$ ranged from 3.6×10^8–5.5×10^{12} molecules cm^{-3} s, the resulting error values were 1.9×10^8–2.4×10^{10} molecules cm^{-3} s.

After obtaining the $OH_{exp,\ dec}$ values, we used Eqs. 2 and 3 to fit the parameters *a*–*f* and *x*–*z* for OFR185 and OFR254 modes, respectively, given that the experimental parameters such as OHR_{ext}, $O_{3,\ out}$, H_2O, and t (in Eq. 2), and r_{O3}, OHR_{ext}, and $O_{3,\ in}$ (in Eq. 3) are known. The $OH_{exp,\ est}$ values were then reconstructed with the fitted parameters and the experimental parameters, and compared with the $OH_{exp,\ dec}$ values via linear regression analysis. Similarly, the error values for all $OH_{exp,\ est}$ values are at least one order of magnitude smaller than the respective $OH_{exp,\ est}$ values. The generation of OH radicals in PAM-OFR is related to the photon fluxes at λ = 185 nm (I_{185}) and λ = 254 nm (I_{254}). According to Rowe et al. (2020), I_{185}:I_{254} is specific to the Hg lamp utilized. Since the OH_{exp} estimation equation for OFR185 uses O_3 concentration as a measurable surrogate for the UV flux at 185 nm, it is also lamp-specific. Because the UV lamps used in our study are different from the BHK lamps employed by Li et al. (2015), we anticipate that the parameters *a*–*f* fitted from our decay experiments (Table S5) should be quite different from those in Li et al. (2015), which is indeed the case. Similarly, fitting parameters *x*–*z* for OFR254 mode from our decay experiments (Table S6) are also different from those in Peng et al. (2015).

3 Results and Discussion

3.1 The OFR185 mode: OHR_{ext} level relevant to ambient conditions

Field studies showed that the environmental OHR_{ext} mainly fluctuated between 10–30 s^{-1} (Fuchs et al., 2017; Lou et al., 2010; Lu et al., 2010; Tan et al., 2018; Yang et al., 2017). To investigate the factors that potentially affect the fitting parameters of Eq. 2 in the estimation of OH_{exp} under ambient conditions, we first performed 16 sets of experiments with OHR_{ext} of 4–23 s^{-1} using SO_2 as the OHR_{ext} source. With the measured $OH_{exp,\ dec}$, the parameters (*a*–*f*) were first derived, which were used to reconstruct $OH_{exp,\ est}$ using Eq. 2 with known OHR_{ext}, ozone concentration ($O_{3,\ out}$), water vapor mixing ratio (H_2O), and residence time (t). The reconstructed $OH_{exp,\ est}$ values were plotted against the $OH_{exp,\ dec}$ values calculated from the trace-gas decay experiments, as shown in Figure 1. The 1:2 and 2:1 lines indicate approximately half an order of magnitude difference between $OH_{exp,\ dec}$ and $OH_{exp,\ est}$, which is considered to be acceptable as an uncertainty in OH_{exp} estimation.

We first investigated the effect of changing residence time on the OH_{exp} estimation. With other experimental parameters (i.e. H_2O, $O_{3,\ out}$, and OHR_{ext}) being similar, we set the residence time to a low value (33 s) and also a range of higher values (61–200 s). The detailed ranges of each experimental condition for different datasets are listed in Table S3. With the residence time of 33 s, the reconstructed $OH_{exp,\ est}$ correlates well with the experimental $OH_{exp,\ dec}$ (slope = 1.061 and R^2 = 0.990, Figure 1a1). The set of fitted parameters *a*–*f* ($FP_{st,\ 185}$; st: short time) applied in Figure 1a1 is presented in Table S5. When the residence time was increased to 61–200 s, the interpolated $OH_{exp,\ est}$ utilizing $FP_{st,\ 185}$ was also in good correlation with $OH_{exp,\ dec}$ (slope = 0.978, R^2 = 0.959, Figure 1a2). We also derived fitted parameters ($FP_{et,\ 185}$; et: extended t) using the data points with the extended range of residence time (33–200 s). Not surprisingly, with the application of $FP_{et,\ 185}$, $OH_{exp,\ est}$ also correlated well with $OH_{exp,\ dec}$ (slope = 0.994, R^2 = 0.955, Figure 1a3). The results indicate that variation in residence time does not significantly affect the fitting parameters of Eq. 2 for the OH_{exp} estimation. From an experimental perspective, since OH_{exp} is the product of OH radical concentration ([OH]) and the residence time (t), as long as the change of t does not significantly alter the quasi-steady-state [OH], the fitted parameters from a narrow range of t should be applicable to situations of longer t. Mathematically, two terms of 180/t and t/180 are related to t, ranging from 0.90–5.45 and 0.18 to 1.11, respectively, which do not contribute significantly to the exponent in Eq. 2 after taking the logarithm of them. It is important to note that the above discussion regarding residence time assumes a plug-flow condition within the PAM-OFR, which is applicable to substances with low $k_{i,\ OH}$, such as SO_2 (or CO). For species that react rapidly with OH, such as monoterpenes or toluene, localized concentration gradients can develop within the OFR, leading to a significant uneven actual RTD that affects the estimation of OH_{exp} (Palm et al., 2018).

Similarly, we then investigated the impacts of H_2O on the estimation of OH_{exp}. Applying fitted parameters from experiments of low water vapor mixing ratios (0.49–0.99 %, Figure 1b1) ($FP_{lH2O,\ 185}$; lH_2O: low H_2O) to data spanning a wide range of water vapor mixing ratios (0.49–2.76 %) also yielded a reasonably good correlation between $OH_{exp,\ est}$ and $OH_{exp,\ dec}$ (Figure 1b2). This could be attributed to the fact that the term $logH_2O$ in Eq. 2 does not contribute significantly to the exponent.

As for ozone concentration, applying fitting parameters ($FP_{lO3,\ 185}$; lO_3: low $O_{3,\ out}$) from experiments of low ozone concentration (1.44×10^{12}–6.79×10^{13} molecules cm^{-3}, Figure 1c1) to reconstruct the data for a wide range (1.44×10^{12}–2.03×10^{15} molecules cm^{-3}) yielded a reasonably good correlation between $OH_{exp,\ est}$ and $OH_{exp,\ dec}$ (Figure 1c2). It only resulted in a mildly increased slope (from 1.063 to 1.272) and similar R^2 values (both are 0.970) as compared to those using the whole ozone concentration range (Figure 1c3).

Ideally, trace-gas decay experiments covering the entire ranges of the t, H_2O, and $O_{3,\ out}$ variations under real experimental conditions should be conducted, which is labor-intensive. Practically, due to the atmospherically relevant variations that occur in t, H_2O, and $O_{3,\ out}$ during the real experiments, the ranges of t, H_2O, and $O_{3,\ out}$ covered by trace-gas decay experiments are usually narrower compared to the real experiments. Our results suggest that the fitting parameters (*a*–*f*) obtained from calibration experiments with relatively narrow ranges of t, H_2O, and $O_{3,\ out}$ can still provide a reliable estimation of OH radical levels during the real experiments, which would cover wider ranges of these conditions.

It is noteworthy that reliable estimations can be achieved regardless of whether the narrow range is situated within the lower or higher interval of the full condition range. Figure 1 demonstrated the case where the narrow range was situated within the lower interval, while Figure S3 presented the case where the narrow range was situated within the higher interval. The detailed ranges of each experimental condition for different datasets are listed in Table S3. As shown in Figure S3, the data points in panel a1 had residence times of 100–296 s, the data points in panel b1 had water vapor mixing ratios of 1.04–2.76 %, and the data points in panel c1 had $O_{3,\,out}$ of 8.45×10^{13}–2.03×10^{15} molecules cm^{-3}. Panels a2, b2, and c2 built on panels a1, b1, and c1 by incorporating data points with shorter t (33–61 s), lower H_2O (0.49–0.97 %), and lower $O_{3,\,out}$ (1.44×10^{12}–6.79×10^{13} molecules cm^{-3}), respectively, but still used fitting parameters *a*–*f* obtained from the higher range of conditions to estimate $OH_{exp,\,est}$. In panels a3, b3, and c3, the parameters *a*–*f* were refitted using all the data points included in the expanded t, H_2O, and $O_{3,\,out}$ ranges, respectively, and the obtained *a*–*f* were used to estimate $OH_{exp,\,est}$. Using panel a1–a3 in Figure S3 as an example, the slope and R^2 values in a2 and a3 were very close to 1, reflecting the good consistency between $OH_{exp,\,est}$ and $OH_{exp,\,dec}$. In the OFR254 mode discussed later (Figure 4, panels c1–c3), this narrower range can also be situated within the middle interval of the full condition range. This applicability of fitting parameters obtained from narrow ranges of experimental conditions is beneficial for quickly obtaining concurrent OH_{exp} during the experiments in field measurements.

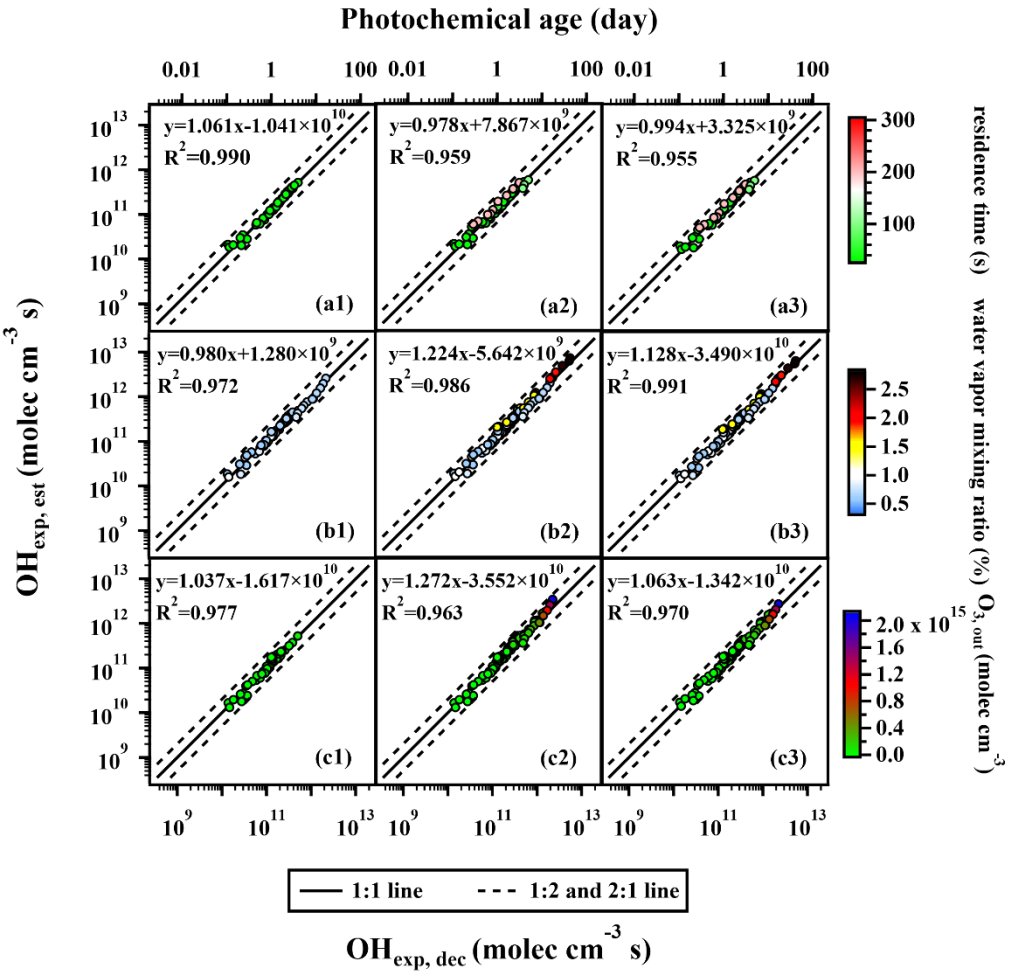

Figure 1: The regression results of $OH_{exp,\ est}$ and $OH_{exp,\ dec}$ when variations occurred in (a1–a3) residence time, (b1–b3) water vapor mixing ratio, and (c1–c3) output O_3 concentration under atmospheric relevant OHR_{ext} level (4–23 s^{-1}). Compared to panels a1, b1, and c1, panels a2, b2, and c2 respectively incorporated additional data points with higher t, H_2O, and $O_{3,\ out}$ values, but still utilized the fitting parameters $FP_{st,\ 185}$, $FP_{lH2O,\ 185}$, and $FP_{lO3,\ 185}$ obtained from the lower condition range to estimate $OH_{exp,\ est}$. In panels a3, b3, and c3, all data points within the extended condition range were used to re-fit the parameters *a–f*, and the resulting $FP_{et,\ 185}$, $FP_{eH2O,\ 185}$, and $FP_{eO3,\ 185}$ were employed to estimate $OH_{exp,\ est}$ (s: short, l: low, e: extended). All the error values for $OH_{exp,\ dec}$ are half or even two orders of magnitude smaller than the corresponding $OH_{exp,\ dec}$ values. When applying a logarithmic scale, the error bars become difficult to represent. To enhance the readability of the graph, error bars have not been included. For the same reason, error bars for $OH_{exp,\ est}$ values are also not displayed.

3.2 The OFR185 mode: OHR_{ext} level relevant to emission sources

The experimental conditions in the PAM-OFR often involve not only general atmospheric conditions (OHR_{ext} < 30 s^{-1}) but also high-concentration conditions, e.g., those directly from emission sources. For instance, the OHR_{ext} of direct vehicle emission can be as high as 1000 s^{-1} with plenty of reducing gases such as CO and VOCs (Nakashima et al., 2010). To evaluate the applicability of Eq. 2 under situations of high OHR_{ext}, we performed high OHR_{ext} (up to 204 s^{-1}) experiments using high

concentrations of SO_2 as the OHR_{ext} source. Compared to the data points shown in Figure 2a (4–23 s^{-1}), Figure 2b and Figure 2c included additional data points with higher OHR_{ext} values (198–204 s^{-1}), while the other conditions remained similar. In Figure 2b, the parameters *a*–*f* ($FP_{lOHR,\ 185}$; lOHR: low OHR_{ext}) obtained from the low-OHR_{ext} data points were used to estimate $OH_{exp,\ est}$, yet those used in Figure 2c were refitted from the data points with extended OHR_{ext} range (4–204 s^{-1}). It could be observed from Figure 2b that when estimating OH_{exp} using $FP_{lOHR,\ 185}$, $OH_{exp,\ est}$ of the high-OHR_{ext} data points were significantly overestimated, with a difference of more than two orders of magnitudes compared to $OH_{exp,\ dec}$. This observation suggests that, different from cases for residence time, water vapor mixing ratio, and ozone concentration shown in the section above, $FP_{lOHR,\ 185}$ were not applicable to high-OHR_{ext} conditions.

We then investigated the possible causes of the discrepancy for OH_{exp} estimation between $FP_{lOHR,\ 185}$ and $FP_{eOHR,\ 185}$ (eOHR: extended OHR_{ext}). From a mathematical perspective, according to Eq. 2, the third term $c \times OHR_{ext}^{d} \times \log(O_{3,\ out} \times 180/t)$ and the fourth term $e \times OHR_{ext}^{f} \times [\log(O_{3,\ out} \times 180/t)]^2$ are associated with OHR_{ext}, which involve fitted parameters of *c*–*f*. To investigate their relationships with OHR_{ext}, we performed a sensitivity test with a fixed ozone concentration (1.77×10^{14} molecules cm^{-3}) and residence time (89 s), which were mean values during our experiments. When using the *c*–*f* values of $FP_{lOHR,\ 185}$ (-0.13922, 0.26786, 0.0026332, and 0.4917), the variations of the third term, the fourth term, and their sum with respect to OHR_{ext} were shown in Figure S4a1–a3, respectively. The third term (Figure S4a1) was negative and decreased as OHR_{ext} increased, while the fourth term (Figure S4a2) was positive and increased as OHR_{ext} increased. The sum of them (Figure S4a3), however, first decreased and then started to increase at approximately OHR_{ext} = 21 s^{-1}, owing possibly to a slower decrease in the third term or a faster increase in the fourth. If contributions from other terms in Eq. 2 were constant, this led to an increase of OH_{exp} as OHR_{ext} increased beyond 21 s^{-1}. Our results showed that the expectation that OH_{exp} should decrease with increasing OHR_{ext} (Li et al., 2015) was applicable to the lower ranges of $OHR_{ext,}$ i.e., under atmospheric relevant conditions. With further increase of OHR_{ext}, i.e., above atmospheric relevant condition, the fitted parameters obtained from the dataset with $FP_{lOHR,\ 185}$ were not applicable.

When using the *c*–*f* values of $FP_{eOHR,\ 185}$ (-0.079114, 0.36805, 0.0041654, and 0.38722), the trends of the third and the fourth terms (Figure S4b1 and S4b2, respectively) were similar to those with low OHR_{ext} (Figure S4a1 and S4a2, respectively); their sum, however, gave a monotonical decreasing trend as OHR_{ext} increased (Figure S4b3), consistent with the expectation that OH_{exp} should decrease with increasing OHR_{ext} (Li et al., 2015). The curve in Figure S4b3 can continue to decrease monotonically at higher OHR_{ext} values, at least until 2000 s^{-1}.

From the perspective of oxidation chemistry, high concentrations of gas phase SO_2 could lead to more SO_2 entering the particle phase. The H_2O_2 in the liquid water of nucleated sulfuric acid aerosols would further oxidize SO_2 (Liu et al., 2020), which could lead to the discrepancy for OH estimation between low OHR and extended high OHR.

Nevertheless, the good agreement between $OH_{exp,\ est}$ and $OH_{exp,\ dec}$ in Figure 2c (using re-fitted parameters from the dataset of extended OHR_{ext}) indicate that Eq. 2 can still be used to estimate OH_{exp} under high-OHR_{ext} conditions. This conclusion is further supported by the results of OH_{exp} obtained using CO as the OHR_{ext} source (see Figure 3 and the section below) under extremely high-OHR_{ext} conditions (up to 1200 s^{-1}). This is advantageous for the use of PAM-OFR in simulations of SOA

formation from direct emission sources (e.g., vehicular exhaust and biomass burning) where OHR_{ext} is extremely high. It is, however, desirable to have OH_{exp} estimated under similarly high OHR_{ext} for those experiments to accurately represent the extent of oxidation.

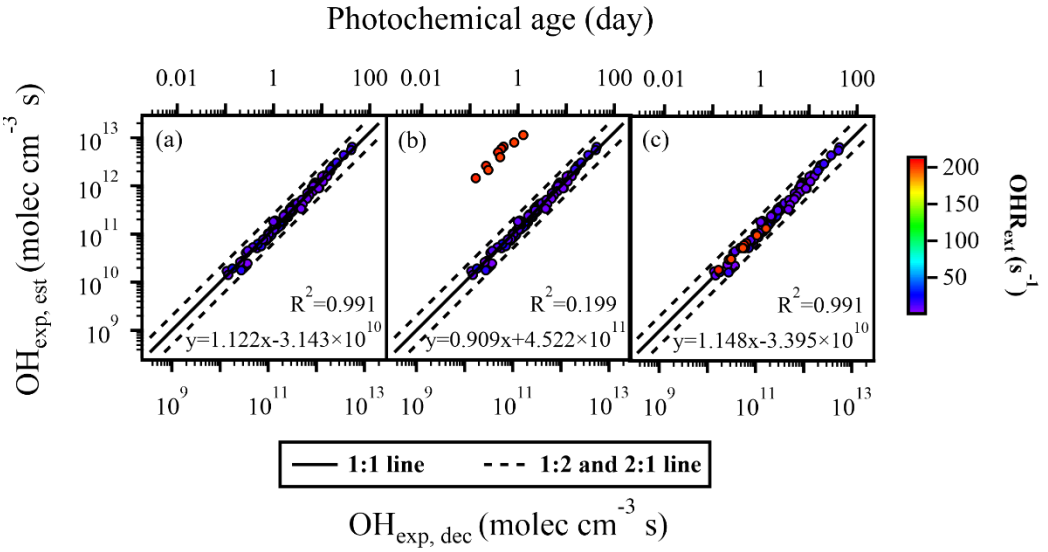

Figure 2: The regression results of $OH_{exp, est}$ and $OH_{exp, dec}$ with different OHR_{ext} levels. In panel a, data points with atmospheric relevant OHR_{ext} level (4–22 s^{-1}) were applied. In addition to the data points contained within panel a, panel b included additional data points with emission sources related OHR_{ext} level (198–204 s^{-1}), but $FP_{lOHR, 185}$ were still used to estimate $OH_{exp, est}$. In panel b, data points in red showed that the $OH_{exp, est}$ of these high-OHR_{ext} data points were significantly overestimated. $FP_{lOHR, 185}$ were not applicable to high-OHR_{ext} conditions. The data points in panel c were identical to those in panel b, but the estimation of $OH_{exp, est}$ utilized the $FP_{eOHR, 185}$ obtained by fitting all data points across the full range of OHR_{ext} levels.

3.3 The OFR185 mode: SO_2 and CO as OHR_{ext} sources

Peng et al. (2015) suggested that SO_2 can better capture the features of real OHR_{ext} decay and effective OHR_{ext}. The reaction between SO_2 and OH is relatively straightforward and is not expected to undergo too many side reactions. CO is a typical gaseous inorganic compound emitted during combustion process. Using CO as an OHR_{ext} source to explore the estimation of OH_{exp} in the simulation of oxidation chemistry for emission sources (i.e., high OHR_{ext} level) is representative. Therefore, we compared the results with SO_2 (Figure 3a) and CO (Figure 3b) as the OHR_{ext} source. When using SO_2 as the OHR_{ext} source, all data points agreed within a factor of 2 (Figure 3a). while only approximately 83 % of the data points agreed within a factor of 2 when CO was used as the OHR_{ext} source (Figure 3b). The deviating data points were mostly concentrated in areas with high OHR_{ext} (> 600 s^{-1}) and low $O_{3, out}$ concentration (10^{12}–10^{13} molecules cm^{-3}), where the removal of CO was relatively low. Li et al. (2015) have observed increased deviations between $OH_{exp, est}$ and $OH_{exp, dec}$, which was attributed, at least in part, to the increased measurement uncertainties for CO when the decrease of its concentration was marginal. We believe that measurement uncertainty might not be the main reason in our case, because most of the decreases in CO concentration during our experiments were larger than the precision of the Picarro G2401 Analyzer (~1.5 ppb at 5 min time resolution). Another

possible reason is that in addition to the reaction with OH radicals, CO may react with some other oxidants, leading to its consumption, while SO_2 was less affected, thereby resulting in more scattered data points for CO. The reaction rate of CO with HO_2 is very slow, and is unlikely to play a significant role ($k_{CO,\ HO2} = 5.55 \times 10^{-27}$ cm^3 $molecule^{-1}$ s^{-1} at 300 K) (You et al., 2007). Cohen and Heicklen (1972) suggested that CO could also react with atomic oxygen ($O(^1D)$). Clerc and Barat (1967) have reported some appreciable rate coefficients (10^{-11} to 10^{-12} cm^3 $molecule^{-1}$ s^{-1}) for the reaction between CO and $O(^1D)$, which are higher than those for the reactions of CO with OH ($k_{CO,\ OH} = 2.4 \times 10^{-13}$ cm^3 $molecule^{-1}$ s^{-1} at 298 K) (Burkholder et al., 2020). It is therefore possible that reaction between CO and $O(^1D)$ might have complicated the decay of CO in the PAM-OFR. To further investigate this aspect, we used the KinSim, a kinetic simulator, to calculate the average mixing ratios of OH, $O(^1D)$, and HO_2 under the specific conditions in the PAM-OFR, and then assessed the relative importance of the reactions CO + OH → CO_2 + H, CO + $O(^1D)$ → CO_2, and CO + HO_2 → CO_2 + OH (Li et al., 2015; Peng and Jimenez, 2019, 2020). The results show that although the reaction rate constant of CO and $O(^1D)$ is 1–2 orders of magnitude higher than that of CO and OH, the concentration of OH is about 6–7 orders of magnitude higher than the concentration of $O(^1D)$, indicating that the reaction of CO with $O(^1D)$ will not have a significant impact on the consumption of CO. The real reason for the scattered data points when using CO in the trace-gas decay experiment is still unknown.

Figure 3c includes the results of trace-gas decay experiments using both SO_2 and CO as the OHR_{ext} source. Despite having different reaction rates with OH radicals, the data points could be collectively utilized to fit the parameters for the estimation equation. With approximately 95 % of the results agreeing within a factor of 2, $OH_{exp,\ est}$ obtained using the fitted parameters exhibited good agreements (slope = 1.101, $R^2 = 0.991$) with $OH_{exp,\ dec}$. Our results thus suggest that although using CO as the OHR_{ext} might result in some scattered data points, it was still feasible to use Eq. 2 to estimate OH_{exp} given that experiments were not done solely in conditions with high OHR_{ext} (i.e., high CO concentrations) and low O_3 concentrations. Another benefit of using CO as OHR_{ext} source for the estimation of OH_{exp} is that it introduces complexity in the precursor, which resembled those in real applications. Although not tested in this study, we also note that further trace-gas decay experiments in the presence of N_2O/NO_x (typical urban environment) should be conducted when oxidation chemistry in the presence of NO_x is studied (Cheng et al., 2021).

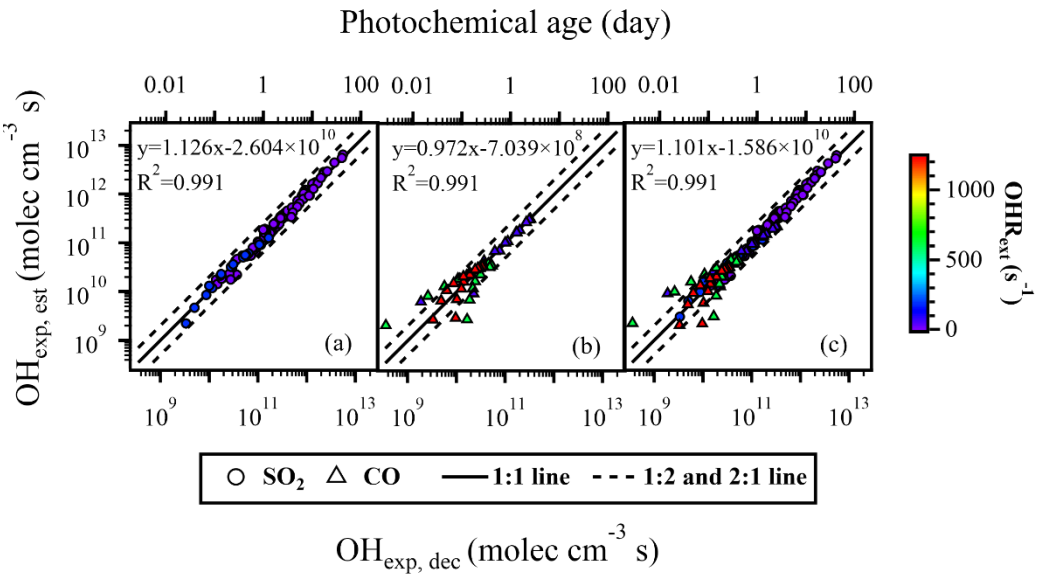

364

365 **Figure 3: The regression results of $OH_{exp,\ dec}$ and $OH_{exp,\ est}$ in the OFR185 mode with (a) SO_2 and (b) CO as OHR_{ext} sources. (c)**
366 **Results from all experiments (using SO_2 and CO) in the OFR185 mode.**

367 **3.4 The OFR254 mode**

368 The equation for OH_{exp} estimation in OFR254 mode is simpler compared to that of OFR185 mode. According to Eq. 3, under
369 OFR254 mode, the three parameters potentially affecting the OH_{exp} are OHR_{ext}, input O_3 concentration, and r_{O3}. The detailed
370 ranges of each experimental condition for different datasets are listed in Table S4. We found that compared to Figure 1, the
371 data points in Figure 4 were more scattered. Most of the R^2 values in Figure 4 were below 0.9, indicating that using SO_2 as the
372 OHR_{ext} source, the estimation of OH_{exp} (using Eq. 3) under the OFR254 mode performed not as well as those under the OFR185
373 mode (using Eq. 2). Firstly, we investigated the impacts of OHR_{ext}. Figure 4a1 showed the regression results of $OH_{exp,\ est}$ and
374 $OH_{exp,\ dec}$ when OHR_{ext} ranged from 5 to 14 s^{-1}. The parameters *x*–*z* ($FP_{lOHR,\ 254}$; lOHR: low external OHR) (Table S6) were
375 obtained by fitting Eq. 3 to $OH_{exp,\ dec}$. In Figure 4a2, the same set of fitted parameters $FP_{lOHR,\ 254}$ from Figure 4a1 were used for
376 a wider range of OHR_{ext} (5–21 s^{-1}). From the regression results (slopes of 1.050 and 1.024, R^2 of 0.890 and 0.894), the same
377 set of parameters yielded similar estimation performance for OH_{exp} despite a wider range of OHR_{ext} in Figure 4a2 compared
378 to that of Figure 4a1. At the same time, these results were not much different from those (slope = 1.071, R^2 = 0.891) using a
379 re-fitted set of parameters ($FP_{eOHR,\ 254}$; eOHR: extended external OHR) for the wider range of OHR_{ext} (Figure 4a3). Even
380 though the correlation was not as good as those in the OFR185 mode, approximately 85 % of the data points agreed within a
381 factor of 2. We did not further extend the OHR_{ext} to values as high as those in the OFR185 mode as discussed above, since the
382 OFR254 mode was much less oxidative and might not be suitable for simulating the oxidation chemistry of extremely high
383 OHR_{ext} as those from direct emissions.

Similarly good correlations were observed when we only used the fitted parameters ($FP_{lO3,\,254}$ and $FP_{mrO3,\,254}$, respectively; lO_3: low $O_{3,\,in}$, mrO_3: medium rO_3) from narrow ranges of input O_3 concentration and r_{O3} (Figure 4b1 and Figure 4c1, respectively) to reconstruct the $OH_{exp,\,est}$ values with extended ranges of these experimental conditions (Figure 4b2 and Figure 4c2, respectively). Such correlations were as good as those with re-fitted parameters ($FP_{eO3,\,254}$ and $FP_{erO3,\,254}$, respectively; eO_3: extended $O_{3,\,in}$, erO_3: extended rO_3) from data points in the extended ranges of O_3 concentration and r_{O3} (Figure 4b3 and Figure 4c3, respectively). These observations thus indicate that under the OFR254 mode, when OHR_{ext}, $O_{3,\,in}$, and r_{O3} vary within certain ranges (5–21 s^{-1}, 6.46 × 10^{13}–4.8 × 10^{14} molecules cm^{-3}, and 0.61–0.99, respectively), Eq. 3 can be used to estimate OH radical levels reasonably well using the fitting parameters (*x*–*z*) obtained from a narrower range of data points.

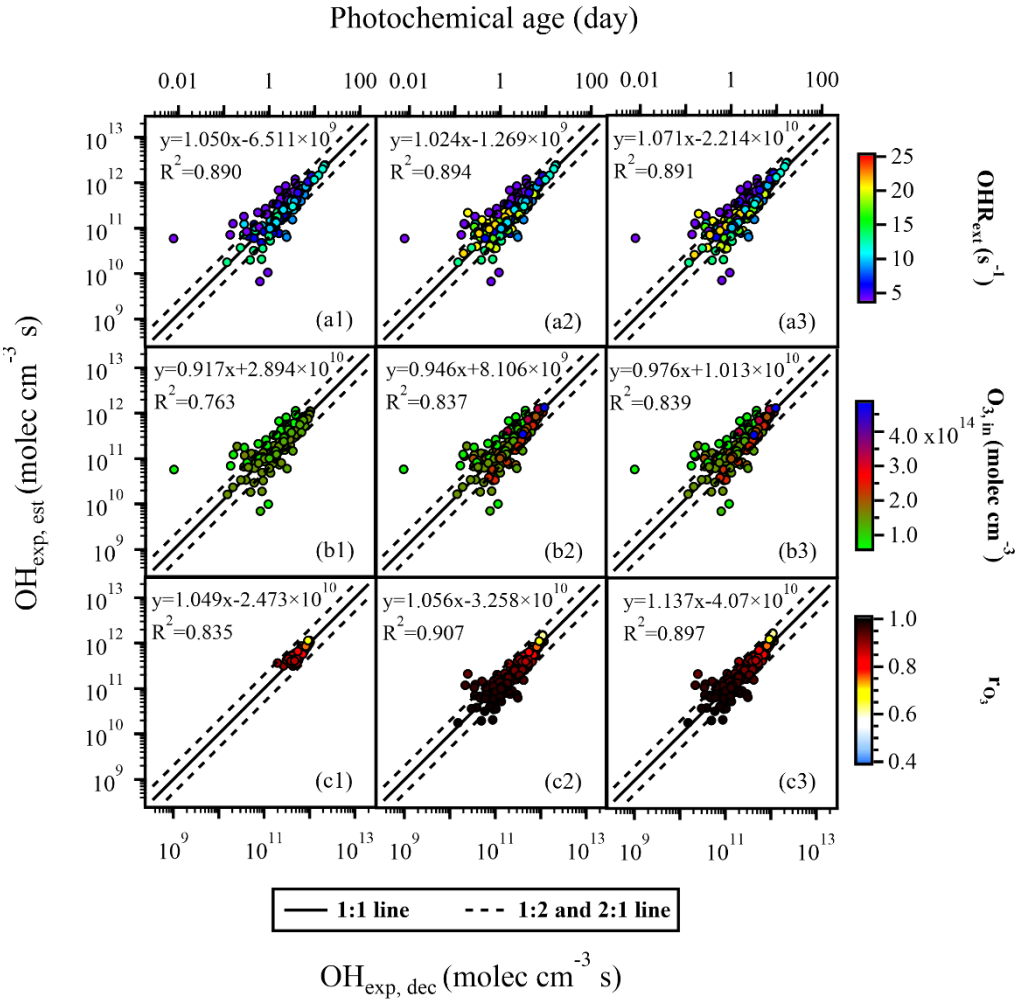

Figure 4: The regression results of $OH_{exp,\,est}$ and $OH_{exp,\,dec}$ when variations occurred in (a1–a3) OHR_{ext}, (b1–b3) input O_3 concentration, and (c1–c3) r_{O3}. Compared to panels a1, b1, and c1, panels a2, b2, and c2 respectively incorporated additional data points with extended OHR_{ext}, $O_{3,\,in}$, and r_{O3} values, but still utilized the fitting parameters $FP_{lOHR,\,254}$, $FP_{lO3,\,254}$, and $FP_{mrO3,\,254}$ obtained from the lower or medium condition range to estimate $OH_{exp,\,est}$. In panels a3, b3, and c3, all data points within the extended

condition range were used to re-fit the parameters *x*–*z*, and the resulting $FP_{eOHR,\ 254}$, $FP_{eO3,\ 254}$, and $FP_{erO3,\ 254}$ were employed to estimate $OH_{exp,\ est}$.

Figure 5a and Figure 5b depicted the correlation between $OH_{exp,\ est}$ estimated from Eq. 3 and $OH_{exp,\ dec}$ calculated from Eq. 1 with SO_2 and CO as OHR_{ext} sources, respectively. When using SO_2 as the OHR_{ext} source, approximately 86 % of the data points agreed within a factor of 2 (Figure 5a). Similar to the case of OFR185, when CO was used as the OHR_{ext} source, the data points were more scattered, with the percentage of data points within a factor of 2 dropping to only about 64 % (Figure 5b). Figure 5c included data points using both SO_2 and CO as the OHR_{ext} sources. Overall, regardless of the OHR_{ext} source, when r_{O3} was higher than 0.93, which meant a low UV intensity, the majority of data points for $OH_{exp,\ est}$ and $OH_{exp,\ dec}$ differed by a factor of two or more. It is therefore recommended that when using the OFR254 mode, too low lamp power settings, for example, UV lamp voltage below 1.5 V should be avoided in the case of our study.

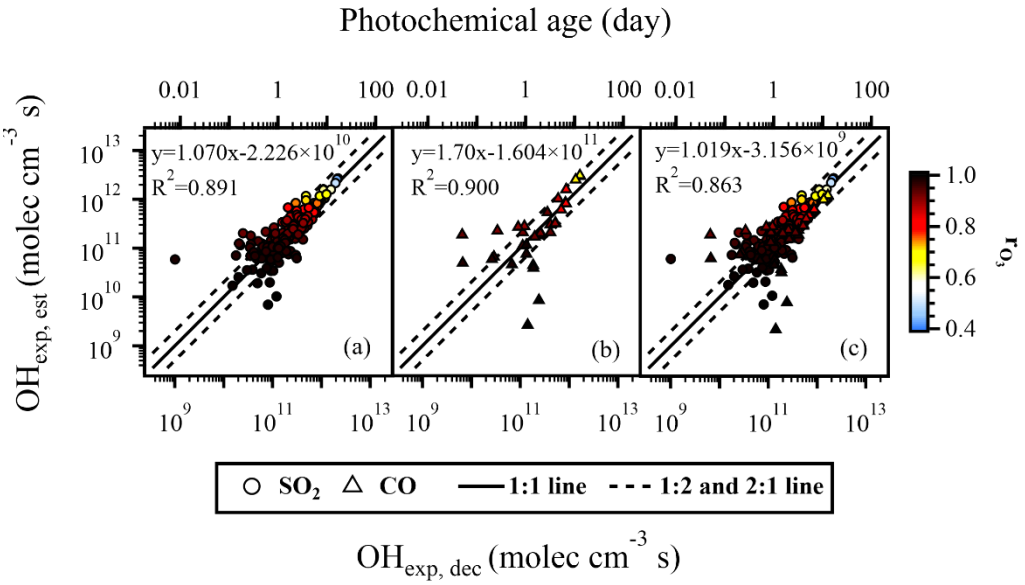

Figure 5: The regression results of $OH_{exp,\ dec}$ and $OH_{exp,\ est}$ in the OFR254 mode with (a) SO_2 and (b) CO as OHR_{ext} sources. (c) Results from all experiments (SO_2 and CO) in the OFR254 mode.

4 Conclusions

A series of OH_{exp} estimation experiments using the PAM-OFR were conducted in OFR185 and OFR254 modes to explore the applicability of the empirical equations under a wide range of conditions. The results indicate that for OFR185 mode, when varying the residence time, water vapor mixing ratio, and output O_3 concentration (as a surrogate for UV intensity) within certain ranges, the empirical equation (Eq. 2) for OH_{exp} proves to be effective in estimating OH_{exp}. Unless there is a significant change in OHR_{ext}, such as transitioning from ambient conditions to emission source conditions, there is no need to re-fit the parameters *a*–*f* in the estimation equation to estimate OH_{exp}. Compared with OFR254 mode, the consistency between $OH_{exp,\ est}$ and $OH_{exp,\ dec}$ in OFR185 mode is better. For the OFR254 mode, when OHR_{ext}, input O_3 concentration, and r_{O3} vary within

certain ranges, the empirical equation (Eq. 3) can be used to estimate OH_{exp} reasonably well using the parameters *x*–*z* obtained from a narrower range of data points. It is important to note that for the OFR185 mode, the above conclusions are valid only if one already has a set of *a*–*f* values that are appropriate for the specific UV lamps being used, as the I_{185}:I_{254} that affects the OH_{exp} is lamp-specific. For a PAM-OFR that employs a different Hg lamp, a series of calibration experiments should be conducted in any case. Alternatively, based on the research by Rowe et al. (2020), the exponential relationship between the *a*–*f* values and the I_{185}:I_{254} could be used to first obtain a set of *a*–*f* values suitable for the UV lamps being used.

To obtain reliable estimates of OH_{exp} using Eqs. 2 and 3 for the OFR185 mode or OFR254 mode, respectively, it is desirable to have sufficient data points (that is, $OH_{exp,\ dec}$ from trace-gas decay experiments) to fit the parameters for the calculation of $OH_{exp,\ est}$. There is currently no consensus on how many data points in trace-gas decay experiments are enough for reliable fitted parameters, which could be important for in-situ OH_{exp} estimation in field studies where a limited number of experiments are done to reduce downtime. We aim to address this by random sampling from the data points in our experiments and determine the minimum number of experiments that are needed to obtain reliable OH_{exp}.

For OFR185 mode, we first used randomly selected N data points from the 175 data points presented previously to fit the parameters (*a*–*f*) using Eq. 2. The fitted parameters were then used to reconstruct $OH_{exp,\ est}$ for all the 175 data points. The $OH_{exp,\ est}$ values were then compared with the corresponding 175 $OH_{exp,\ dec}$ values. This procedure was repeated 10 times for each N, with N starting from 7 till approximately 50 (Figure 6a). The average R^2, slope, and intercept from the 10 attempts were then shown as a function of N for experiments with SO_2 only (Figure 6a) and those with SO_2 and CO (Figure 6b). It can be observed that around 30 data points are needed for experiments with SO_2 only while around 20 data points are needed to have stable R^2 values and slopes when using both SO_2 and CO. For OFR254 mode, the same procedure was applied to the 241 data points. It was not surprising that the results were a lot more scattered (Figure 6c and Figure 6d) compared to those for OFR185 mode given their performance shown in the previous section. Nevertheless, our analysis suggests that around 25 data points are needed to obtain reliable $OH_{exp,\ est}$ for OFR254 mode, whether SO_2 alone (Figure 6c) or SO_2 and CO (Figure 6d) are used for the trace-gas decay experiments. Therefore, despite the limitation that this practice only randomly samples the data points without considering the range of any experimental conditions, our analysis suggests that 20–30 data points are normally needed to obtain reliable OH_{exp} for both OFR185 and OFR254 modes.

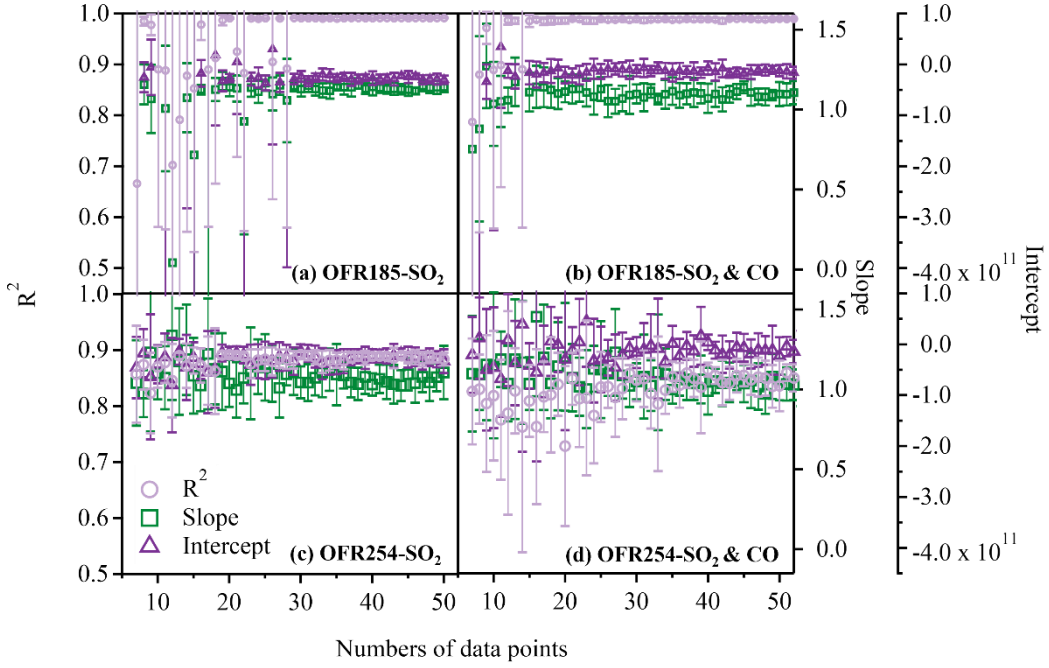

Figure 6: The regression results of $OH_{exp,\ dec}$ and $OH_{exp,\ est}$ (characterized by the R^2, slope, and intercept) when different numbers of data points were chosen. (a) SO_2 as OHR_{ext} source in OFR185 mode, (b) SO_2 or CO as OHR_{ext} source in OFR185 mode, (c) SO_2 as OHR_{ext} source in the OFR254 mode, and (d) SO_2 or CO as OHR_{ext} source in the OFR254 mode.

Our study suggests that the $OH_{exp,\ est}$ estimated from the empirical equations agrees better with $OH_{exp,\ dec}$ for the OFR185 (Figure 3) than for the OFR254 mode (Figure 5). This can be understood from the perspective of OH generation and its consumption by OHR_{ext} (Li et al., 2015). For the OFR185 mode, there are two pathways to generate OH radicals: the photolysis of H_2O and the photolysis of O_3. For the OFR254 mode, the main pathway for OH radical generation is solely the photolysis of O_3. Consequently, when OHR_{ext} changes, the disruption to OH_{exp} in the system is more significant in the case of the OFR254 mode, while the OH_{exp} in the OFR185 mode remains more stable. In addition, pseudo-first-order kinetics between OH radicals and SO_2 or CO is assumed, with [OH] being at a pseudo-steady state. Yet, the relatively low OH radical generation capacity in the OFR254 mode might not necessarily always fulfil such an assumption, leading to higher uncertainties for estimating OH_{exp}. Therefore, the OFR185 mode offers certain advantages such as relatively high OH_{exp}, more accurate OH_{exp} estimation, as well as no external input of O_3 needed. However, for substances that exhibit strong absorption at the wavelength of 185 nm and are prone to photolysis, such as aromatic species (Peng et al., 2016), using the OFR254 mode is a better choice. For users of other OFRs (non-PAM-OFR) who would like to apply the conclusions above, at least two conditions must be met: (1) the concentration of [OH] within the OFR should remain stable, and (2) the assumption of plug flow conditions is acceptable, allowing for the neglect of differences in the actual RTD, heterogeneity in the UV light intensity and the concentration of

radicals/oxidants at different points within the reactor, which are caused by different designs of reactors (such as wall materials, shapes, or volumes).

Data availability

The data shown in the paper are available on request from the corresponding authors (huangdd@saes.sh.cn and yongjieli@um.edu.mo).

Supplement link

The supplement related to this article is available online at:

Author contribution

QL, DDH, and YJL conceived and planned the experiments. QL and YW carried out the experiments. QL, DDH, and YJL analysed the data and took the lead in writing the paper. QL, DDH, YJL, ATL, and XC contributed to the interpretation of the results. SL, LZ, CYH, ST, QC, KIH, HW, KMM, and CH provided significant input during the revision of the manuscript. All authors provided feedback on the paper.

Competing interests

The authors declare no competing interests.

Acknowledgements

Dan Dan Huang acknowledges the financial support from the National Key Research and Development Program of China (2022YFC3703600), the Science and Technology Commission of Shanghai Municipality (21230711000) and the General Fund of Natural Science Foundation of China (42275124). Yong Jie Li acknowledges the financial support from Science and Technology Development Fund, Macau SAR (File No. 0031/2023/AFJ and 0107/2023/RIA2) and multiyear research grants (No. MYRG-GRG2023-00008-FST-UMDF and MYRG-GRG2024-00032-FST-UMDF) from the University of Macau.

References

Atkinson, R. and Arey, J.: Atmospheric degradation of volatile organic compounds, Chem. Rev., 103, 4605-4638, doi: 10.1021/cr0206420, 2003.

Atkinson, R., Baulch, D. L., Cox, R. A., Crowley, J. N., Hampson, R. F., Hynes, R. G., Jenkin, M. E., Rossi, M. J., and Troe, J.: Evaluated kinetic and photochemical data for atmospheric chemistry: Volume II–gas phase reactions of organic species, Atmos. Chem. Phys., 6, 3625-4055, doi: 10.5194/acp-6-3625-2006, 2006.

Barmet, P., Dommen, J., DeCarlo, P., Tritscher, T., Praplan, A., Platt, S., Prévôt, A., Donahue, N., and Baltensperger, U.: OH clock determination by proton transfer reaction mass spectrometry at an environmental chamber, Atmospheric Measurement Techniques, 5, 647-656, 2012.

Burkholder, J. B., Sander, S. P., Abbatt, J. P. D., Barker, J. R., Cappa, C., Crounse, J. D., Dibble, T. S., Huie, R. E., Kolb, C. E., Kurylo, M. J., Orkin, V. L., Percival, C. J., Wilmouth, D. M., and Wine, P. H.: Chemical kinetics and photochemical data for use in atmospheric studies, Evaluation Number 19, Pasadena, CA: Jet Propulsion Laboratory, National Aeronautics and Space Administration, http://jpldataeval.jpl.nasa.gov, 2020.

Cao, J., Wang, Q., Li, L., Zhang, Y., Tian, J., Chen, L. A., Ho, S. S. H., Wang, X., Chow, J. C., and Watson, J. G.: Evaluation of the oxidation flow reactor for particulate matter emission limit certification, Atmos. Environ., 224, 117086, doi: 10.1016/j.atmosenv.2019.117086, 2020.

Cheng, X., Chen, Q., Jie Li, Y., Zheng, Y., Liao, K., and Huang, G.: Highly oxygenated organic molecules produced by the oxidation of benzene and toluene in a wide range of OH exposure and NOx conditions, Atmos. Chem. Phys., 21, 12005-12019, doi: 10.5194/acp-21-12005-2021, 2021.

Cheng, X., Li, Y. J., Zheng, Y., Liao, K., Koenig, T. K., Ge, Y., Zhu, T., Ye, C., Qiu, X., and Chen, Q.: Oxygenated organic molecules produced by low-NOx photooxidation of aromatic compounds: contributions to secondary organic aerosol and steric hindrance, Atmos. Chem. Phys., 24, 2099-2112, doi: 10.5194/acp-24-2099-2024, 2024.

Clerc, M. and Barat, F.: Kinetics of CO formation studied by far-UV flash photolysis of CO2, J. Chem. Phys., 46, 107-110, doi: 10.1063/1.1840358, 1967.

Cocker, D. R., Flagan, R. C., and Seinfeld, J. H.: State-of-the-art chamber facility for studying atmospheric aerosol chemistry, Environ. Sci. Technol., 35, 2594-2601, doi: 10.1021/es0019169, 2001.

Cohen, N. and Heicklen, J.: The Oxidation of Inorganic Non-metallic Compounds, in: Reactions of Non-Metallic Inorganic Compounds, Compr. Chem. Kinet., 1-137, doi: 10.1016/s0069-8040(08)70303-0, 1972.

Ehhalt, D. H.: Photooxidation of trace gases in the troposphere Plenary Lecture, Phys. Chem. Chem. Phys., 1, 5401-5408, doi: 10.1039/A905097C, 1999.

Friedman, B. and Farmer, D. K.: SOA and gas phase organic acid yields from the sequential photooxidation of seven monoterpenes, Atmos. Environ., 187, 335-345, doi: 10.1016/j.atmosenv.2018.06.003, 2018.

Fuchs, H., Tan, Z., Lu, K., Bohn, B., Broch, S., Brown, S. S., Dong, H., Gomm, S., Häseler, R., and He, L.: OH reactivity at a rural site (Wangdu) in the North China Plain: contributions from OH reactants and experimental OH budget, Atmos. Chem. Phys., 17, 645-661, doi: 10.5194/acp-17-645-2017, 2017.

George, I. J., Vlasenko, A., Slowik, J. G., Broekhuizen, K., and Abbatt, J. P. D.: Heterogeneous oxidation of saturated organic aerosols by hydroxyl radicals: uptake kinetics, condensed-phase products, and particle size change, Atmos. Chem. Phys., 7, 4187-4201, doi: 10.5194/acp-7-4187-2007, 2007.

Hildebrandt, L., Donahue, N. M., and Pandis, S. N.: High formation of secondary organic aerosol from the photo-oxidation of toluene, Atmos. Chem. Phys., 9, 2973-2986, doi: 10.5194/acp-9-2973-2009, 2009.

Kang, E., Root, M. J., Toohey, D. W., and Brune, W. H.: Introducing the concept of potential aerosol mass (PAM), Atmos. Chem. Phys., 7, 5727-5744, doi: 10.5194/acp-7-5727-2007, 2007.

Lambe, A. T., Ahern, A. T., Williams, L. R., Slowik, J. G., Wong, J. P. S., Abbatt, J. P. D., Brune, W. H., Ng, N. L., Wright, J. P., and Croasdale, D. R.: Characterization of aerosol photooxidation flow reactors: heterogeneous oxidation, secondary organic aerosol formation and cloud condensation nuclei activity measurements, Atmos. Meas. Tech., 4, 445-461, doi: 10.5194/amt-4-445-2011, 2011.

Li, R., Palm, B. B., Ortega, A. M., Hlywiak, J., Hu, W., Peng, Z., Day, D. A., Knote, C., Brune, W. H., and De Gouw, J. A.: Modeling the radical chemistry in an oxidation flow reactor: Radical formation and recycling, sensitivities, and the OH exposure estimation equation, J. Phys. Chem. A, 119, 4418-4432, doi: 10.1021/jp509534k, 2015.

Liao, K., Chen, Q., Liu, Y., Li, Y. J., Lambe, A. T., Zhu, T., Huang, R.-J., Zheng, Y., Cheng, X., and Miao, R.: Secondary organic aerosol formation of fleet vehicle emissions in China: Potential seasonality of spatial distributions, Environ. Sci. Technol., 55, 7276-7286, doi: 10.1021/acs.est.0c08591, 2021.

Liu, J., Chu, B., Chen, T., Liu, C., Wang, L., Bao, X., and He, H.: Secondary organic aerosol formation from ambient air at an urban site in Beijing: effects of OH exposure and precursor concentrations, Environ. Sci. Technol., 52, 6834-6841, doi: 10.1021/acs.est.7b05701, 2018.

Liu, T., Clegg, S. L., and Abbatt, J. P.: Fast oxidation of sulfur dioxide by hydrogen peroxide in deliquesced aerosol particles, Proceedings of the National Academy of Sciences, 117, 1354-1359, 2020.

Lou, S., Holland, F., Rohrer, F., Lu, K., Bohn, B., Brauers, T., Chang, C. C., Fuchs, H., Häseler, R., and Kita, K.: Atmospheric OH reactivities in the Pearl River Delta–China in summer 2006: measurement and model results, Atmos. Chem. Phys., 10, 11243-11260, doi: 10.5194/acp-10-11243-2010, 2010.

Lu, K., Zhang, Y., Su, H., Brauers, T., Chou, C. C., Hofzumahaus, A., Liu, S. C., Kita, K., Kondo, Y., and Shao, M.: Oxidant (O3 + NO2) production processes and formation regimes in Beijing, J. Geohys. Res.: Atmospheres, 115, doi: 10.1029/2009JD012714, 2010.

Mao, J., Ren, X., Brune, W. H., Olson, J. R., Crawford, J. H., Fried, A., Huey, L. G., Cohen, R. C., Heikes, B., and Singh, H. B.: Airborne measurement of OH reactivity during INTEX-B, Atmos. Chem. Phys., 9, 163-173, doi: org/10.5194/acp-9-163-2009, 2009.

Nakashima, Y., Kamei, N., Kobayashi, S., and Kajii, Y.: Total OH reactivity and VOC analyses for gasoline vehicular exhaust with a chassis dynamometer, Atmos. Environ., 44, 468-475, doi: 10.1016/j.atmosenv.2009.11.006, 2010.

Ono, R., Nakagawa, Y., Tokumitsu, Y., Matsumoto, H., and Oda, T.: Effect of humidity on the production of ozone and other radicals by low-pressure mercury lamps, J Photochem Photobiol, A, 274, 13-19, doi: 10.1016/j.jphotochem.2013.09.012, 2014.

Palm, B. B., de Sá, S. S., Day, D. A., Campuzano-Jost, P., Hu, W., Seco, R., Sjostedt, S. J., Park, J.-H., Guenther, A. B., and Kim, S.: Secondary organic aerosol formation from ambient air in an oxidation flow reactor in central Amazonia, Atmospheric Chemistry and Physics, 18, 467-493, 2018.

Pan, T., Lambe, A. T., Hu, W., He, Y., Hu, M., Zhou, H., Wang, X., Hu, Q., Chen, H., and Zhao, Y.: A comprehensive evaluation of enhanced temperature influence on gas and aerosol chemistry in the lamp-enclosed oxidation flow reactor (OFR) system, Atmospheric Measurement Techniques Discussions, 2023, 1-34, 2023.

Peng, Z. and Jimenez, J. L.: KinSim: a research-grade, user-friendly, visual kinetics simulator for chemical-kinetics and environmental-chemistry teaching, J. Chem. Educ, 96, 806– 811, doi: 10.1021/acs.jchemed.9b00033, 2019.

Peng, Z. and Jimenez, J. L.: Radical chemistry in oxidation flow reactors for atmospheric chemistry research, Chem. Soc. Rev., 49, 2570-2616, doi: 10.1039/C9CS00766K, 2020.

Peng, Z., Day, D. A., Stark, H., Li, R., Lee-Taylor, J., Palm, B. B., Brune, W. H., and Jimenez, J. L.: HOx radical chemistry in oxidation flow reactors with low-pressure mercury lamps systematically examined by modeling, Atmos. Meas. Tech., 8, 4863-4890, doi: 10.5194/amt-8-4863-2015, 2015.

Peng, Z., Day, D. A., Ortega, A. M., Palm, B. B., Hu, W., Stark, H., Li, R., Tsigaridis, K., Brune, W. H., and Jimenez, J. L.: Non-OH chemistry in oxidation flow reactors for the study of atmospheric chemistry systematically examined by modeling, Atmos. Chem. Phys., 16, 4283-4305, doi: 10.5194/acp-16-4283-2016, 2016.

Rowe, J. P., Lambe, A. T., and Brune, W. H.: Effect of varying the λ=185 and 254 nm photon flux ratio on radical generation in oxidation flow reactors, Atmos. Chem. Phys., 20, 13417-13424, doi: 10.5194/acp-20-13417-2020, 2020.

Seinfeld, J. H. and Pandis, S. N.: Atmospheric chemistry and physics: from air pollution to climate change, John Wiley & Sons, Inc., ISBN 9781119221166, 2016.

Stone, D., Whalley, L. K., and Heard, D. E.: Tropospheric OH and HO2 radicals: field measurements and model comparisons, Chem. Soc. Rev., 41, 6348-6404, doi: 10.1039/C2CS35140D, 2012.

Tan, Z., Fuchs, H., Lu, K., Hofzumahaus, A., Bohn, B., Broch, S., Dong, H., Gomm, S., Häseler, R., and He, L.: Radical chemistry at a rural site (Wangdu) in the North China Plain: observation and model calculations of OH, HO2 and RO2 radicals, Atmos. Chem. Phys., 17, 663-690, doi: 10.5194/acp-17-663-2017, 2017.

Tan, Z., Rohrer, F., Lu, K., Ma, X., Bohn, B., Broch, S., Dong, H., Fuchs, H., Gkatzelis, G. I., and Hofzumahaus, A.: Wintertime photochemistry in Beijing: observations of RO x radical concentrations in the North China Plain during the BEST-ONE campaign, Atmos. Chem. Phys., 18, 12391-12411, doi: 10.5194/acp-18-12391-2018, 2018.

Wang, N., Zannoni, N., Ernle, L., Bekö, G., Wargocki, P., Li, M., Weschler, C. J., and Williams, J.: Total OH reactivity of emissions from humans: in situ measurement and budget analysis, Environ. Sci. Technol., 55, 149-159, doi: 10.1021/acs.est.0c04206, 2020.

Wang, X., Liu, T., Bernard, F., Ding, X., Wen, S., Zhang, Y., Zhang, Z., He, Q., Lü, S., and Chen, J.: Design and characterization of a smog chamber for studying gas-phase chemical mechanisms and aerosol formation, Atmos. Meas. Tech., 7, 301-313, doi: 10.5194/amt-7-301-2014, 2014.

Yang, Y., Shao, M., Keßel, S., Li, Y., Lu, K., Lu, S., Williams, J., Zhang, Y., Zeng, L., and Nölscher, A. C.: How the OH reactivity affects the ozone production efficiency: case studies in Beijing and Heshan, China, Atmos. Chem. Phys., 17, 7127-7142, doi: 10.5194/acp-17-7127-2017, 2017.

You, X., Wang, H., Goos, E., Sung, C.-J., and Klippenstein, S. J.: Reaction kinetics of CO + HO2→ products: ab initio transition state theory study with master equation modeling, J. Phys. Chem. A, 111, 4031-4042, doi: 10.1021/jp067597a, 2007.

Zhang, Z., Xu, W., Lambe, A. T., Hu, W., Liu, T., and Sun, Y.: Insights Into Formation and Aging of Secondary Organic Aerosol From Oxidation Flow Reactors: A Review, Curr. Pollut. Rep., 1-14, doi: 10.1007/s40726-024-00309-7, 2024.